# Calorimetric evidence of nodal gaps in the nematic superconductor FeSe

Frédéric Hardy,[1,*] Mingquan He,[2,1,†] Liran Wang,[1,3] Thomas Wolf,[1] Peter Schweiss,[1] Michael Merz,[1] Maik Barth,[1]
Peter Adelmann,[1] Robert Eder,[1] Amir-Abbas Haghighirad,[1,4] and Christoph Meingast[1]
[1]*Institute for Solid-State Physics, Karlsruhe Institute of Technology, 76021 Karlsruhe, Germany*
[2]*Chongqing Key Laboratory of Soft Condensed Matter Physics and Smart Materials, College of Physics, Chongqing University, Chongqing 401331, People's Republic of China*
[3]*Kirchhoff Institute of Physics, Heidelberg University, INF 227, 69120 Heidelberg, Germany*
[4]*Clarendon Laboratory, Department of Physics, University of Oxford, Parks Road, Oxford OX1 3PU, United Kingdom*

(Received 20 July 2018; revised manuscript received 10 January 2019; published 29 January 2019)

Superconductivity in FeSe has recently attracted a great deal of attention because it emerges out of an electronic nematic state of elusive character. Here we study both the electronic normal state and the superconducting gap structure using heat-capacity measurements on high-quality single crystals. The specific-heat curve, from 0.4 K to $T_c = 9.1$ K, is found to be consistent with a recent gap determination using Bogoliubov quasiparticle interference [P. O. Sprau *et al.*, Science **357**, 75 (2017)]; however, only if nodes are introduced on either the electron or the hole Fermi-surface sheets. Our analysis, which is consistent with quantum-oscillation measurements, relies on the presence of one hole and one electron band only, and thus the fate of the theoretically predicted second electron pocket remains mysterious.

DOI: 10.1103/PhysRevB.99.035157

## I. INTRODUCTION

In cuprate and iron pnictide superconductors, there are strong indications that pairing is magnetically mediated, i.e., by the exchange of spin fluctuations [1–3]. A key ingredient to identify the pairing mechanism is to study the momentum dependence of the superconducting gap, $\Delta\,(\mathbf{k})$. In both materials, $\Delta\,(\mathbf{k})$ changes sign between $\mathbf{k}$ and $\mathbf{k}' = \mathbf{k} + \mathbf{Q}$, where $\mathbf{Q}$ denotes the momentum at which the spin fluctuation–mediated pairing interaction is peaked. Whereas, in cuprates, the sign change occurs for $\mathbf{Q} = (\pi, \pi)$, leading to a $d_{x^2-y^2}$ state, $\mathbf{Q}$ connects hole and electron Fermi-surface sheets in pnictides, giving rise to an $s\pm$ state [1–3].

Unlike in pnictides, long-range magnetism is absent in FeSe, although strong magnetic fluctuations exist at low temperature [4]. Here, superconductivity emerges from a nematic state that breaks the $C_4$ symmetry below $T_s \simeq 90$ K. Nematicity manifests itself as a dramatic orbital-dependent shrinking of the Fermi surface [5] in the presence of strong orbital-selective spin fluctuations [6]. Orbital selectivity could also be relevant for superconductivity as first pointed out by Agterberg *et al.* for $Sr_2RuO_4$ [7], i.e., Cooper pairing predominantly binds electrons that share the same orbital character, leading to a highly anisotropic, possibly even nodal order parameter.

Experimentally and theoretically, there is an emerging consensus for extremely anisotropic gaps in FeSe. Using low-temperature Bogoliubov quasiparticle interference and scanning tunneling microscopy (BQPI/STM), Sprau *et al.* [8] found that $\Delta\,(\mathbf{k})$ is highly anisotropic, but nodeless, on both electron and hole pockets with $\Delta_{\max}/\Delta_{\min} \gtrsim 15$, more or less consistent with heat-capacity data [9]. The Fermi surface averaged gaps on the electron and hole pockets are of nearly equal magnitude but opposite in sign, i.e., $\langle\Delta_h\rangle_k = 1.5$ meV and $\langle\Delta_e\rangle_k = -1.2$ meV [8]. Angle-resolved photoemission spectroscopy (ARPES) measurements [10–13] confirm the strong gap anisotropy but are inconclusive about the existence of line nodes due to the slightly higher temperature ($T > 1.8$ K) of the measurements. Both ARPES [11,13] and BQPI/STM [8], however, agree that $\Delta\,(\mathbf{k})$ is maximal (minimal) on the portions of the Fermi surface where the $d_{yz}$ ($d_{xz}$ and $d_{xy}$) orbital weight is dominant. These results were explained theoretically either by invoking orbital-selective correlations [8,14], pairing in the presence of nematic orbital ordering [15], or nematic pairing from orbital selective spin fluctuations [16]. On the other hand, thermal-transport [17,18], penetration-depth [19,20], and heat-capacity studies [21–24] all reported essentially a strong two-band behavior with $\delta = \frac{\langle\Delta_h(k)\rangle_k}{\langle\Delta_e(k)\rangle_k} \approx 3-10$.

In this paper, we report a detailed thermodynamic study of seven different batches of FeSe single crystals, grown by chemical vapor transport (CVT), as a function of temperature and magnetic field. We argue that the Sommerfeld coefficient $\gamma_n$ within the nematic phase is consistent with a Fermi surface that consists of only one hole and one electron band in agreement with recent ARPES measurements [25], instead of the three pockets expected theoretically [14–16]. Excellent agreement of our specific heat can be obtained using the anisotropic gaps derived from the BQPI/STM data [8,26]; however, only if one of the pockets exhibits line nodes. This nodal behavior is supported by the field dependence of the mixed-state heat capacity. Further, it is found to be surprisingly robust against disorder. Finally, similar to $BaFe_2As_2$ [27], we find an anomalous linear temperature-dependent

---

[*] frederic.hardy@kit.edu

[†] mingquan.he@cqu.edu.cn

2469-9950/2019/99(3)/035157(11)

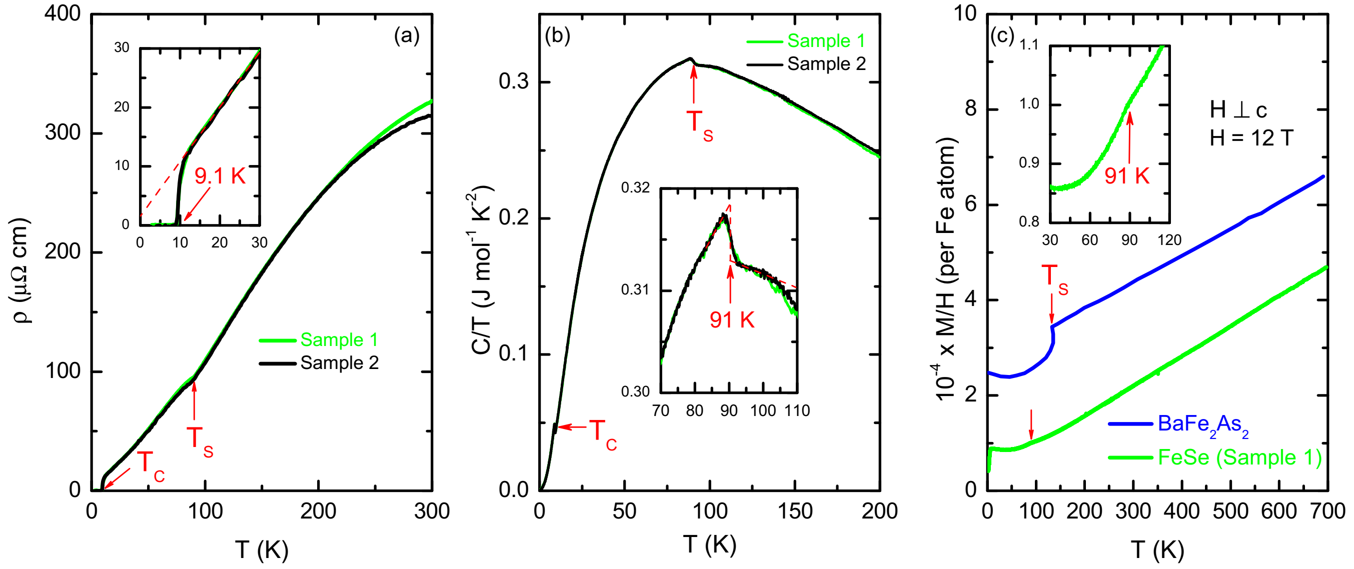

FIG. 1. (a) Resistivity of samples 1 and 2. The inset shows a magnification of the low-temperature region. The dashed line is a linear extrapolation of the normal-state resistivity to $T = 0$. (b) Heat capacity of samples 1 and 2. (c) Comparison of the magnetic susceptibility of sample 1 to that of $BaFe_2As_2$ reproduced from Ref. [27]. In (b) and (c), the insets show data around $T_S = 91$ K on an enlarged scale.

susceptibility from $T > T_S$ to 700 K, a feature that appears to be a hallmark of the undoped Fe-based superconductors.

## II. SAMPLE CHARACTERIZATION

Figures 1(a)–1(b) show the temperature dependence of the resistivity and specific heat of samples 1 and 2, which are characteristic of our best crystals. The quite large residual resistivity ratio, $\mathrm{RRR} \equiv \frac{\rho(300\mathrm{K})}{\rho(0\mathrm{K})} \approx 200$, in comparison to previous studies [8,9,18,22,28,29], is an indication of a high crystal quality. A clear steplike anomaly related to nematicity is observed at $T_s = 91$ K.

Figure 2(a) demonstrates that the low-temperature electronic heat capacity $C_e(T)/T$ of samples 1 and 2 is practically identical to that of two other single crystals, all grown under similar conditions. We find a sharp superconducting transition at $T_c \approx 9.1$ K, with a width of 0.7 K and $\Delta C_e/\gamma_n T_c \approx 1.75$ indicative of weak-to-moderate coupling. Details about the sample preparation and the lattice subtraction are given in Appendices A and B, respectively. Superconductivity is almost fully suppressed for $H = 14$ T, revealing a temperature-independent $C_e/T$ for $T < 12$ K [see Fig. 2(a)] indicative of a nematic Landau Fermi liquid despite the nearly linear resistivity [see Fig. 1(a)]. The Sommerfeld coefficient $\gamma_n \equiv \frac{C_e}{T}$ amounts reproducibly to $6.9 \pm 0.1\,\mathrm{mJ\,mol^{-1}\,K^{-2}}$ within the nematic normal state. We note that $\gamma_n$ is almost equal to that of $BaFe_2As_2$ deep inside the spin-density-wave phase [30].

## III. EVIDENCE FOR NODAL EXCITATIONS

A simple inspection of the data shown in Fig. 2(a) suggests that both electron and hole gaps are comparable in magnitude, since the typical low-temperature humplike feature of superconductors with both small and large gaps, as found, e.g., in $MgB_2$ [31] and $KFe_2As_2$ [32] (see Appendix C), is missing in the FeSe data. This is consistent with the gaps derived from both BQPI/STM and ARPES [8,12,13] but not with the strong two-band character inferred from both penetration-depth [19] and thermal-conductivity measurements [18]. For $T \leqslant 2$ K, $C_e/T$ decreases linearly with temperature [see inset of Fig. 2(a)] and extrapolates at $T = 0$ to a negligibly small residual density of states $0 \leqslant \gamma_0 < 0.2\,\mathrm{mJ\,mol^{-1}\,K^{-2}}$ which amounts to less than 3% of $\gamma_n$. This linear behavior represents clear evidence for the existence of line nodes in our FeSe crystals. Our data are substantially different from all previous specific-heat measurements. In particular, an excess specific heat was observed for $T < 4$ K in Refs. [9,22,24,29,33], which was interpreted as a signature of a tiny energy gap. In Appendix D, we show that a more likely explanation involves a Schottky anomaly from paramagnetic impurities. Besides, the 1 K anomaly, reported by Chen *et al.* [9], is only observed in two of our crystals measured under special conditions and therefore may not represent an intrinsic feature of FeSe.

## IV. MIXED-STATE SPECIFIC HEAT

Further evidence for the existence of nodes can be obtained by examining the field dependence of $\gamma(T, H) \equiv C_e(T, H)/T$ at low temperature in the mixed state depicted in Fig. 2(b). Indeed, Volovik [34–37] showed that $\gamma(T, H)$ is proportional to $\gamma_n\sqrt{H}$ far from the upper critical field $H_{c2}$, i.e., for $\frac{T}{T_c} \ll \sqrt{\frac{H}{H_{c2}}}$, in nodal superconductors due to the Doppler shift experienced by the delocalized quasiparticles with momentum near the nodal directions. As illustrated in the inset of Fig. 2(b), this is effectively the case, e.g., for samples 1 and 5 for $\frac{T}{T_c} < 0.15\sqrt{\frac{H}{H_{c2}}}$, indicative of nodal gaps. On the other hand, for $H/H_{c2} > 0.4$ [Fig. 2(b)], we find that $\gamma(T, H)$ follows a quasilinear field dependence, which is anomalous for an orbitally limited nodal superconductor. As mentioned in Ref. [23], this is most likely related to sizable paramagnetic

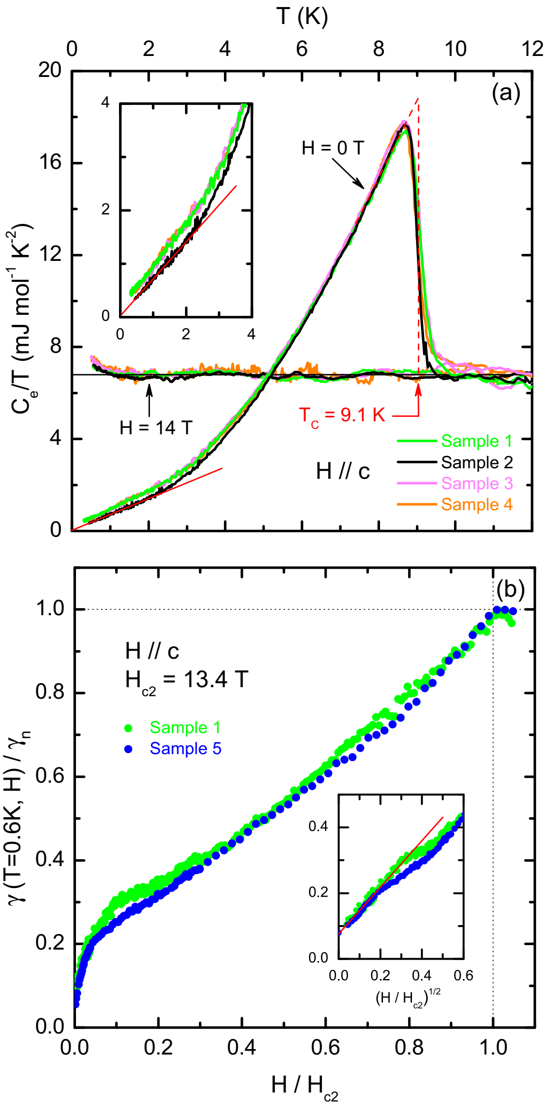

FIG. 2. (a) Low-temperature $C_e(T)$ of samples 1, 2, 3, and 4 in 0 and 14 T. The dashed line represents an entropy–conserving construction that yields $T_c \approx 9.1$ K. The inset shows the low-temperature data on an enlarged scale, revealing a linear $C_e/T$ for $T \leqslant 2$ K indicative of line nodes (solid line). (b) Mixed-state heat capacity $\gamma(T, H)$ of samples 1 and 5 at $T = 0.6$ K. The inset shows $\gamma(T, H)$ as a function of $H^{1/2}$ in the low-field region.

effects [23,38,39], since the Pauli limiting field, $H_p = \frac{\sqrt{2}\Delta}{g\mu_B}$, is estimated to be of the order of 18 T in FeSe.

## V. COMPARISON WITH QUASIPARTICLE-INTERFERENCE MEASUREMENTS

In the following, we make a direct comparison of our heat-capacity measurements with that calculated using the BQPI/STM measurements. We use the data of sample 2 with a near-zero value of $\gamma_0$. In Fig. 3(a), we reproduce the angular dependence of $\Delta_{h,e}(\phi)$ inferred from the BQPI/STM experiments (solid symbols) [8] together with our fits (solid lines) using the leading angular harmonic approximation [1,15], as done in Ref. [9]. The resulting heat capacity, computed within the two-band $\alpha$-model [31], is compared to our measurements in Figs. 3(b)–3(c) (red lines). Here, we impose equal density of states on both bands as inferred from our analysis of the quantum-oscillation data (see Appendix E), so that in principle there are no fit parameters. $C_e/T$ derived from the BQPI/STM gap structure reproduces our data very well, but only down to $T/T_c \approx 0.3$. Below this temperature, the calculation underestimates the specific heat, reflecting the existence of low-lying nodal excitations in our crystals [see Fig. 3(c)]. To improve the agreement at low temperature, we modify our fit of $\Delta_{h,e}(\phi)$ to allow for the possibility of line nodes on either the hole or the electron band, as displayed in Figs. 3(d) and 3(g) (red areas), respectively. In both cases, the calculations shown, respectively, in Figs. 3(e)–3(f) and 3(h)–3(i), are now in excellent agreement with our measurements over the entire temperature range. This provides another strong indication for the existence of line nodes in FeSe. This is also consistent with the recent calculations of Benfatto *et al.*[16], which predict nodes only on the electron pocket. Finally, the possibility of line nodes on both bands appears to be ruled out [see Figs. 3(j)–3(l)] since the calculation now overestimates the measured specific heat for $T/T_c < 0.3$.

## VI. EFFECT OF DISORDER

Next, we discuss the role of disorder on the gap structure by comparing $C_e(T)$ of several single crystals grown under different conditions (see Appendix A). Although no discernible changes in composition could be resolved using x-ray diffraction, significant differences are observed in our specific-heat measurements (see Fig. 4). First, a substantial reduction of $T_c$ of about 7% and 14% is found for samples 5 and 6, respectively, indicating that disorder is sizably pair-breaking. This is in line with the observation that scattering by Fe vacancies [40] and twin boundaries [26] produces in-gap bound states in FeSe. Similarly, the normalized specific-heat anomaly, $\frac{\Delta C}{\gamma_n T_c}$, is reduced significantly from 1.73 in sample 1 to 1.26 in sample 6, indicating that $\langle\Delta_{h,e}\rangle_k$ are also reduced by defect scattering. The linear $C_e/T$ at low temperature is quite robust and persists in all samples in spite of the significant reduction of both $T_c$ and $\frac{\Delta C}{\gamma_n T_c}$ (see inset of Fig. 4). This result is quite surprising, because significant interband scattering is expected to produce sizable gapless excitations for a sign-changing order parameter [41,42].

## VII. NEMATIC FERMI SURFACE AND CORRELATIONS

The exact electronic structure in the nematic state of FeSe is still highly disputed. Theoretically, one expects to have one hole and two electron bands [8,14–16], but ARPES spectra, however, have been interpreted as providing evidence for either one or two electron bands [5,6,12,25,43]. Clearly, the present heat-capacity simulations need only two bands to accurately describe $C_e(T)$ for $T < T_c$, which is consistent with the BQPI/STM data [8] and one of the ARPES measurements [13]. Further, the absence of a sizable $\gamma_0$ excludes the possibility of an additional electron band, either gapless or with a very small gap, with any sizable weight [44]. Our analysis of the quantum-oscillation data [45], which yields $\gamma_n$ of 5.7 and 9.4 mJ mol$^{-1}$ K$^{-2}$ in two- and three-band models, respectively (see Appendix E), also appears to favor a

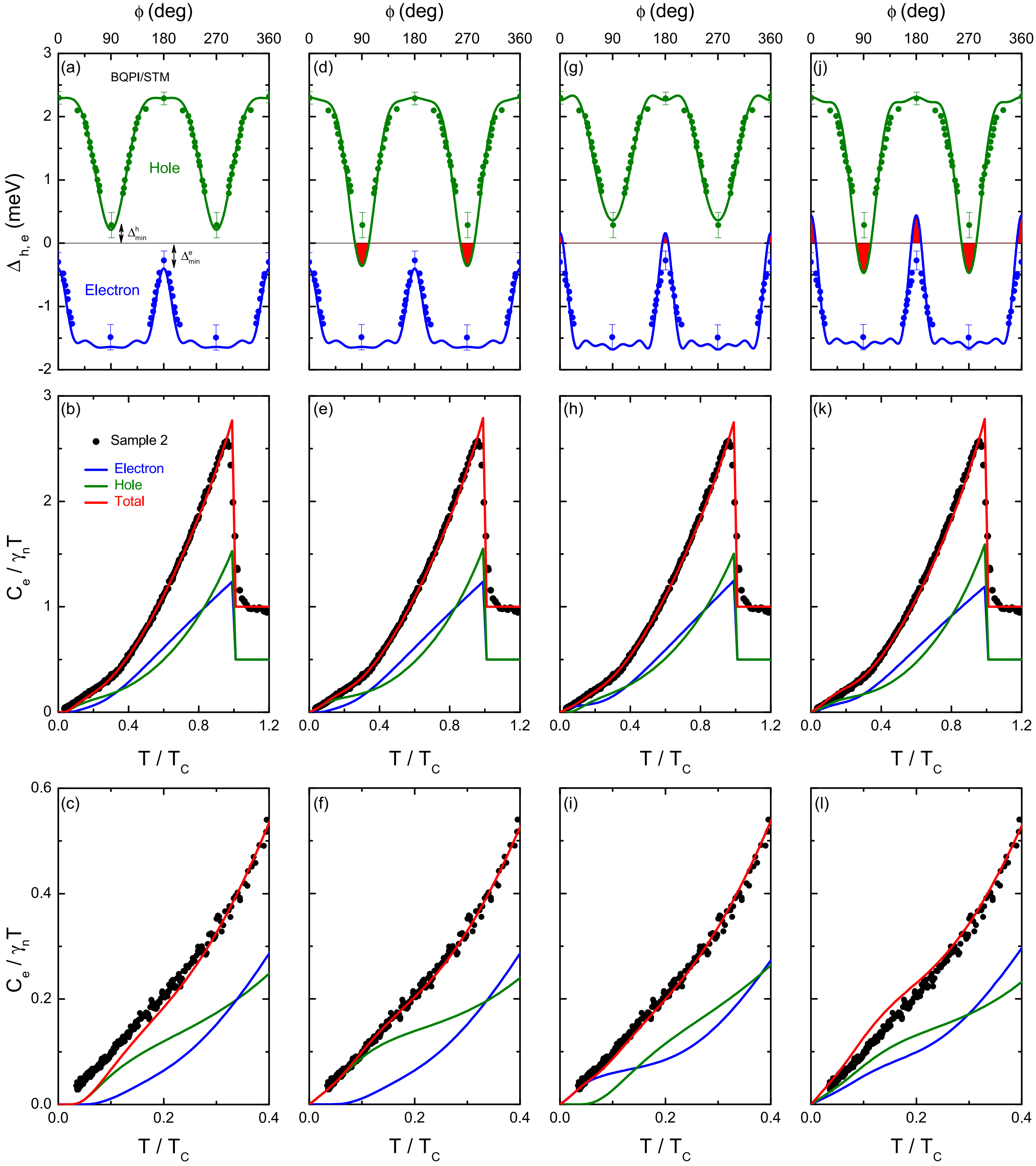

FIG. 3. (a) Angle-resolved nodeless hole and electron superconducting gaps, $\Delta_{h,e}(\phi)$, reported by BQPI/STM [8] (green and blue symbols, respectively). $\phi$ is measured with respect to the $a$ orthorhombic axis. (d), (g), (j) Nodal gap structures used for heat-capacity calculations. Solid lines are fits within the leading angular harmonic approximation. (b), (e), (h), (k) Comparison of the heat capacity (red line) calculated using the gap structures shown in panels (a), (d), (g), (j), respectively, to the measured $C_e(T)$ of sample 2. (c), (f), (i), (l) show the respective low-temperature part on an enlarged scale. The green and blue lines are the individual hole and electron heat-capacity contributions, respectively.

two-band scenario, since the inferred $\gamma_n$ value is closer to the measured one. The two-band value is just 17% smaller than our direct measurement. For comparison, similar calculations in BaFe$_2$As$_2$ and KFe$_2$As$_2$ [32,46], for which the Fermi surface is fully determined, lead to comparable deviations of about 11 and 13%, respectively.

In Refs. [8,14], it is argued that the second electron band is not observed because it may be quite incoherent as a

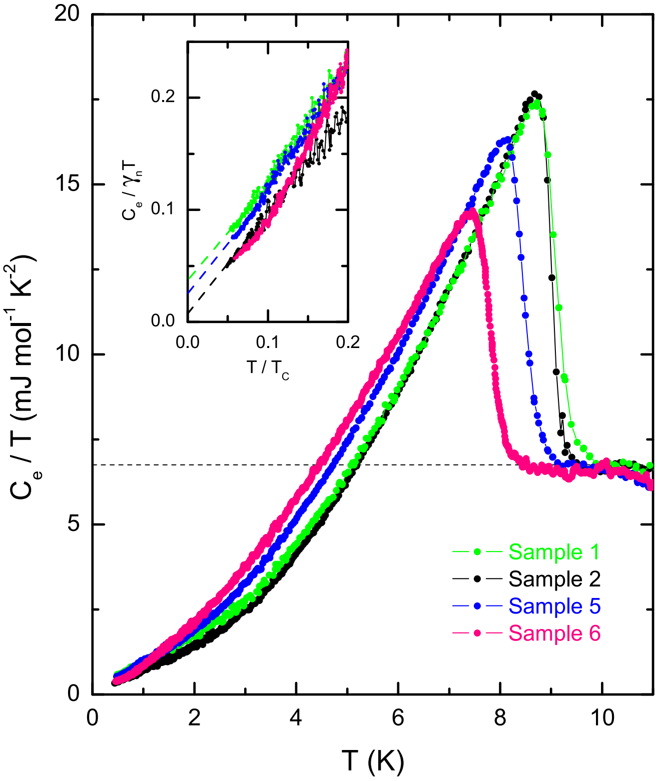

FIG. 4. (a) $C_e(T)$ of samples 1, 2, 5, and 6 with different amounts of disorder. The inset shows the low-temperature part in normalized units on an enlarged scale.

result of strong local correlations. However, in AFe$_2$ As$_2$ ($A =$ K, Rb, Cs) in which the $d$ bands are closer to half-filling with strongly enhanced correlations [47,48], one finds (i) quite heavy but still coherent bands with $m^* > 20m_e$ ($m_e$ is the bare electron mass) [49], (ii) a Sommerfeld coefficient exceeding 100 mJ mol$^{-1}$ K$^{-2}$, and (iii) a remarkable coherence-incoherence crossover [50,51] indicative of strong orbital-selective correlations [47,50–52]. In FeSe, we find no evidence for such a crossover in the magnetic susceptibility [see Fig. 1(c)] although the resistivity exhibits a broad maximum around 400 K [53]. Instead, the susceptibility of FeSe increases linearly from $T > T_s$ to at least 700 K with the same slope as BaFe$_2$ As$_2$ [27]. Thus, the scenario of a completely incoherent second electron band appears rather unlikely and a better understanding of the nematic state is required to explain the missing electron pocket.

## VIII. CONCLUSIONS

In conclusion, we have reported a detailed study of the thermodynamic properties of FeSe single crystals. We consistently find a linear electronic specific heat $C_e/T$ for $T \ll T_c$ indicative of the bulk existence of line nodes. This nodal behavior is found to be quite robust and remarkably persists in samples with significantly depressed $T_c$. Our results are consistent with a two-band scenario, i.e., a Fermi surface that consists of one hole and one electron pocket only. The fate of the theoretically predicted second electron band remains unclear and must be related to the elusive nature of the nematic state.

## ACKNOWLEDGMENTS

We thank Laura Fanfarillo, Rafael Fernandes, Andrey Chubukov, Christophe Marcenat, Thierry Klein, Peter Hirschfeld, Andreas Kreisel, Brian Andersen, Matthew Watson, Paul Wiecki, and Antony Carrington for fruitful discussions. M.H. acknowledges support by the Fundamental Research Funds for the Central Universities (2018CD-JDWL0011), China. L.W. acknowledges support by Deutsche Forschungsgemeinschaft (DFG) Funding No. WA4313/1-1. A.-A.H acknowledges the financial support of the Oxford Quantum Materials Platform Grant No. EP/M020517/1. The contribution from M.M. was supported by the Karlsruhe Nano Micro Facility (KNMF).

## APPENDIX A: EXPERIMENTAL METHODS

FeSe single crystals were grown by CVT [54,55]. Fe and Se powders were mixed in the proportions given in Table I and sealed in a fused silica ampoule together with a eutectic mixture of KCl and AlCl$_3$. Table I also indicates the source ($T_1$) and sink ($T_2$) temperatures of the two-zone furnace. In the last three columns, we indicate the mass, composition, and $T_c$ of the individual single crystals taken from each batch and studied in this paper.

Wavelength dispersive x-ray spectroscopy typically reveals an impurity level below 500 ppm. There is no evidence for contamination by Cl, Si, K, or Al impurities. The composition was determined by structural refinement of single-crystal x-

TABLE I. The first six columns summarize the nominal composition and the growth conditions for seven different batches. In the last three columns, we indicate the mass, composition, and T$_c$ of the single crystal taken from each batch and studied in this paper.

| Batch | Nominal composition | | | Growth conditions | | | Characterization | | |
|---|---|---|---|---|---|---|---|---|---|
| | Fe mass (g) | Fe:Se molar ratio | KCl : AlCl$_3$ mass (g) | $T_1$ (°C) | $T_2$ (°C) | Duration (days) | Sample mass (mg) | Composition | T$_c$ (K) |
| #1 | 4.3 | 1.1:1.0 | 10.4 | 383 | 340 | 32 | 2.13 | - | 9.1 |
| #2 | 1.1 | 1.1:1.0 | 7.99 | 390 | 330 | 35 | 4.29 | Fe$_{0.993(8)}$Se | 9.1 |
| #3 | 4.3 | 1.1:1.0 | 10.4 | 401 | 349 | 33 | 1.18 | Fe$_{0.996(4)}$Se | 9.1 |
| #4 | 4.3 | 1.1:1.0 | 10.4 | 391 | 295 | 27 | 1.2 | Fe$_{0.999(8)}$Se | 9.1 |
| #5 | 2.46 | 1.1:1.0 | 19.8 | 447 | 299 | 28 | 5.43 | - | 8.45 |
| #6 | 2.01 | 1.2:1.0 | 5.7 | 390 | 240 | 22 | 6.62 | Fe$_{0.997}$Se | 8.24 |
| #7 | 1.68 | 1.2:1.0 | 11.4 | 380 | 164 | 32 | 4.11 | - | 7.78 |

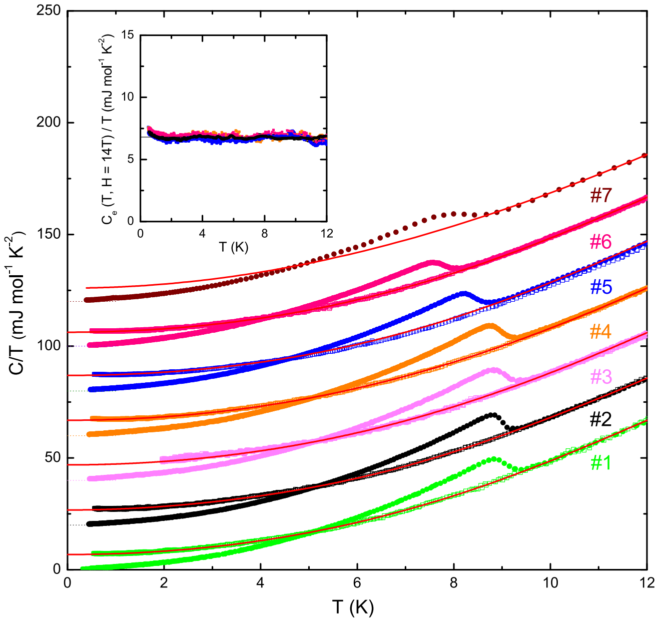

FIG. 5. Temperature dependence of the specific heat of the seven single crystals discussed in this paper in 0 T (closed symbols) and 14 T (open symbols) for H ∥ c. For clarity, curves are vertically shifted from each other by 20 mJ mol$^{-1}$ K$^{-2}$. Red curves represent fits to the 14 T data using Eq. (B1). The inset shows the resulting electronic heat capacity for $H = 14$ T.

ray diffraction data (four-circle and image plate) of a small piece of each crystal with an uncertainty of about 1% in composition (see Table I). No indications for interstitial atoms were found. X-ray powder diffraction confirms the absence of second phases, particularly of unreacted $\alpha$-Fe and Fe$_7$Se$_8$. The extremely small level of impurities and defects (less than one impurity per 2000 Fe atoms) are confirmed by STM topography [56]. $T_c$ was determined via specific-heat measurements.

Electrical contacts with typical resistances of around 2 Ω were made using silver paste, and the sample resistance was measured by a four-point method. Magnetization measurements were carried out in a Physical Property Measurement System (PPMS) using the vibrating sample magnetometer unit from Quantum Design Inc. Specific heat was measured with the PPMS using the thermal-relaxation method [57] for field-sweep measurements and the dual-slope method [58,59] for temperature-sweep measurements.

## APPENDIX B: DERIVATION OF THE LATTICE SPECIFIC HEAT

Figure 5 shows the low-temperature specific heat of the seven single crystals discussed in this paper, in 0 and 14 T for $H \parallel c$. We find that superconductivity is fully suppressed, at least down to 0.4 K, in a field of 14 T. Thus, a reliable phonon background can be obtained by least-square fitting the 14 T-data between 14 and 0.8 K (red lines in Fig. 5) to

$$C(T, H = 14T) = \gamma_n T + B_3 T^3 + B_5 T^5 + B_7 T^7, \qquad \text{(B1)}$$

where $C_e(T) = \gamma_n T$ and $C_{\text{lat}}(T) = B_3T^3 + B_5T^5 + B_7T^7$ represent the electronic and the field-independent lattice contributions, respectively. Here $\gamma_n$ is the Sommerfeld coefficient and $C_{\text{lat}}(T)$ is expressed within the harmonic-lattice approximation, where $B_3$ is the prefactor of the $T^3$ term from Debye theory [60]. The inferred values of $\gamma_n$ and $B_n$, with $n = \{3, 5, 7\}$, are given in Table II and compared to values from previous published results which were all derived from data measured in 9 T, i.e., in a field where superconductivity is not fully suppressed, $T_c$ (9 T) ≈3.8 K. As argued in Ref. [61], this could lead to significant errors in the determination of the lattice heat capacity and can partly explain the differences shown in Table II.

The resulting electronic contributions $C_e(T, H) = C(T, H) - C_{\text{lat}}(T)$ for $H = 0$ and 14 T, which fulfill entropy conservation, are shown in Figs. 7 and 5 (inset), respectively. In our case, we confirm that $\gamma_n$ is both field and sample independent.

## APPENDIX C: COMPARISON TO OTHER MULTIBAND SUPERCONDUCTORS

In Fig. 6, we compare the electronic specific heat of FeSe to that of the well-known strong multiband superconductors KFe$_2$As$_2$ [32] and MgB$_2$ [31], which exhibit a value of the ratio of the large to the small gap $\delta = \frac{<\Delta_L(k)>_k}{<\Delta_S(k)>_k}$ (where $\langle \ldots \rangle_k$ denotes the average over the Fermi surface) of about 8.6 and 3.7, respectively. These values are similar to $\delta \approx 10$ and 3 reported by heat-transport [18] and penetration-depth [19] measurements for FeSe, respectively. We find that the prominent steep increase of $C_e/T$ at low temperature observed for both KFe$_2$As$_2$ and MgB$_2$ (see arrows in Fig. 6), which typically occurs when $k_BT$ becomes of the order of the smaller gap $\Delta_S(T)$, is absent in FeSe. Instead, the curve appears single gapped for FeSe and $C_e/T$ gradually increases, indicating that the two gaps are actually comparable in magnitude, contrary

TABLE II. The first line indicates the fit parameters obtained by fitting our 14 T data (shown in Fig. 5) to Eq. (B1). The values indicated next to ± represent the sample-to-sample deviation, not the statistical error. The following lines are literature results obtained from curves measured in $H = 9$ T for which superconductivity is not fully suppressed.

| Composition | $T_c$ (K) | $\gamma$ (mJ mol$^{-1}$ K$^{-2}$) | $B_3$ (mJ mol$^{-1}$ K$^{-4}$) | $B_5$ (mJ mol$^{-1}$ K$^{-6}$) | $B_7$ (mJ mol$^{-1}$ K$^{-8}$) | Method, [Ref.] |
|---|---|---|---|---|---|---|
| Fe$_{0.994(4)}$Se | 9.1 - 7.78 | 6.9(±0.1) | $0.38 \pm 0.01$ | $(5.9 \pm 1.4) \times 10^{-4}$ | $(-2.9 \pm 1.1) \times 10^{-6}$ | CVT, this work |
| Fe$_{1.01(2)}$Se | 8.5 | 5.43 | 0.463 | $-2.82 \times 10^{-4}$ | - | Solid-state, [33,62] |
| Fe$_{1.037}$Se | 8.11 | 5.73 | 0.421 | - | - | KCl : AlCl$_3$ flux, [21] |
| - | 8.2 | 5.82 | 0.4624 | $-2.6 \times 10^{-4}$ | - | CVT, [9] |
| Fe$_{0.99(1)}$Se | 8.4 | 6.5 | 0.365 | $1.94 \times 10^{-4}$ | - | CVT, [22,63,64] |
| Fe$_{1.005}$Se | 8.7 | 6.86 | 0.37 | 0.001 | $-5.72 \times 10^{-6}$ | CVT, [24,65] |

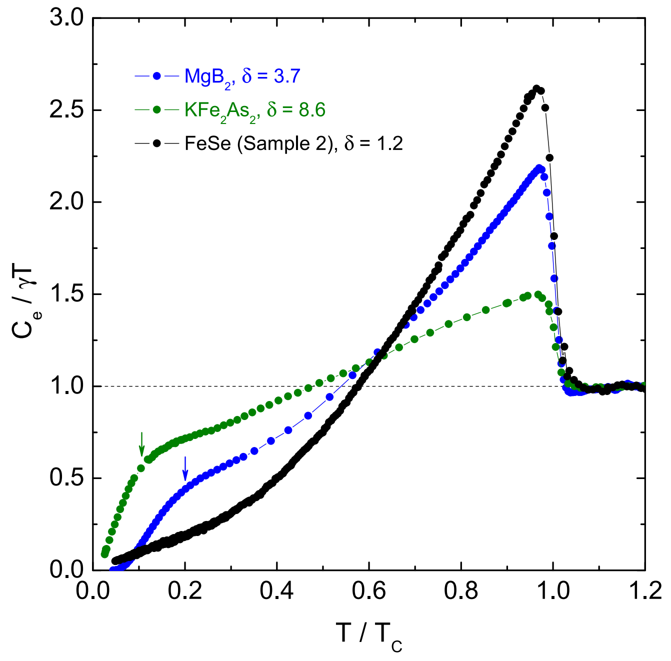

FIG. 6. Comparison of $C_e(T)$ of FeSe to that of multiband superconductors $MgB_2$ and $KFe_2As_2$ taken from Refs. [31,32]. The arrow indicates the hump related to the small gaps $\Delta_S(T)$, i.e., where $\Delta_S(T) \approx k_BT$.

to both penetration-depth [19] and thermal-conductivity [18] measurements. However, our results agree quite well with the average values $\langle\Delta_h\rangle_k = 1.5$ meV and $\langle\Delta_e\rangle_k = 1.2$ meV inferred from both BQPI/STM and ARPES measurements for the hole and electron bands, respectively [8,12].

## APPENDIX D: COMPARISON TO PUBLISHED RESULTS

In Fig. 7, we compare $C_e(T)$ from the literature to our data. We find that there exist sizable differences between our measurements and those of several different groups, despite comparable values of $T_c$. A large excess heat capacity, with respect to our data, is notably observed for $T < 2$ K in polycrystals obtained by solid-state synthesis [33] shown in gray in Figs. 7(d)–7(e). These samples, with $Fe_{1.01(2)}Se$, are not single phase and were found to contain $\alpha$-Fe, $Fe_7Se_8$ and $\delta$-FeSe [33,62]. Contamination by either $Fe_7Se_8$ or $\alpha$-FeSe could explain the different values of $\gamma_n$ and $B_3$ with respect to that of CVT-grown samples (see Table II). However, the hump below 2 K [gray curves in Figs. 7(d)–7(e)] likely arises from paramagnetic impurities (e.g., Fe). This extra contribution persists but progressively vanishes in the higher-$T_c$ crystals of Jiao *et al.* [22] and Sun *et al.*[24] but remains absent from our data, as illustrated in Figs. 7(c) and 7(b), respectively. Similar paramagnetic contributions were also observed in $Ba_{1-x}K_xFe_2As_2$ around 2–3 K and were represented by a field-dependent approximation to a Schottky function [61].

In zero field, the Schottky contribution of noninteracting impurities ideally vanishes for any $T > 0$. However, for interacting paramagnetic centers, the heat capacity exhibits a characteristic maximum at $T_{\rm max} \approx 0.42\theta_{\rm Sch}$ where $\theta_{\rm Sch}$ measures the internal interaction field between impurities in zero magnetic field. In Figs. 7(b)–7(c), we show an estimation of the Schottky contribution for the crystals of Jiao *et al.* [22] and Sun *et al.*[24], respectively, using

$$C_{\rm sch}(T,n) = n\left(\frac{\theta_{\rm Sch}}{T}\right)^2 \frac{e^{\frac{\theta_{\rm Sch}}{T}}}{\left(e^{\frac{\theta_{\rm Sch}}{T}}+1\right)^2}, \tag{D1}$$

where $n$ is the concentration of impurities. We used $\Theta_{\rm Sch} = 3$ K and $n = 350$ ppm ($n = 100$ ppm) for the sample of Jiao *et al.* [22] (Sun *et al.*[24]). The resulting difference $C_e(T) - C_{\rm Sch}(T,n)$ matches quite nicely our data for sample 5 as shown in Fig. 7(f). Thus, the hump around 2 K, which was initially interpreted as the signature of a small superconducting energy gap in Refs. [22,24], is probably due to several hundreds ppm of paramagnetic impurities. This amount is in good agreement with the value of 300 ppm $\alpha$-Fe inferred from magnetization measurements [22,63].

Figure 7(a) shows a comparison of the heat capacity of sample 1 with that of Sato *et al.* [23] obtained by the quasiadiabatic heat-pulse method. Both crystals exhibit similar values of $T_c$ and $\Delta C_e/T_c$ but the curves strongly differ for $T < 8$ K. Here, the difference might be related to a lack of adiabaticity of the method used in Ref. [23] inherent to the smallness of the FeSe crystals and the very small value of the Sommerfeld coefficient.

In Figure 7(e), we compare the specific heat of sample 7 to that of Chen *et al.* [9]. Similarly, we observe a steplike anomaly around 1 K (see inset) which was interpreted in Ref. [9] as an antiferromagnetic phase transition in FeSe below $T_c$. This is shown in Fig. 8(a) on an enlarged view. We observe a similar anomaly for sample 2, which exhibits a much larger $T_c$ value, but only when the measurement is performed upon slow cooling from 20 K to 0.4 K. However, for faster cooling rates, this anomaly completely disappears. Although the origin of this anomaly remains unexplained, our results suggest that this anomaly may not represent an intrinsic property of FeSe single crystals.

In Fig. 8(b), we show the mixed-state specific heat of FeSe reported by Sun *et al.* [24]. An initial steep increase of $C/T$ is observed up to $H \approx 1$ T followed by a quasi field-independent specific heat for $1 < H < 4$ T. For larger fields, $C/T$ increases continuously to $H_{c2}$. In Ref. [24], it is argued that this three-stage behavior is related to the existence of three energy gaps. This result is quite different from our data in sample 1 [light green curve in Fig. 8(b)], which shows a smooth increase of $C/T$ to $H_{c2}$. However, it qualitatively agrees with the erroneous heat capacity of sample 1 (dark green curve in Fig. 8(b)) obtained when the field dependence of the addenda, shown in Fig. 8(c) (dark yellow), is not taken into account.

## APPENDIX E: ANALYSIS OF QUANTUM-OSCILLATION DATA

In Tables III and IV, we summarize the results of quantum-oscillation measurements from Ref. [45] obtained in continuous magnetic fields ($H < 35$ T). Similar results were obtained in Refs. [67–69] in pulsed fields ($H < 80$ T). We show hereafter that these data can be analyzed within two different scenarios: a two- and a three-band model.

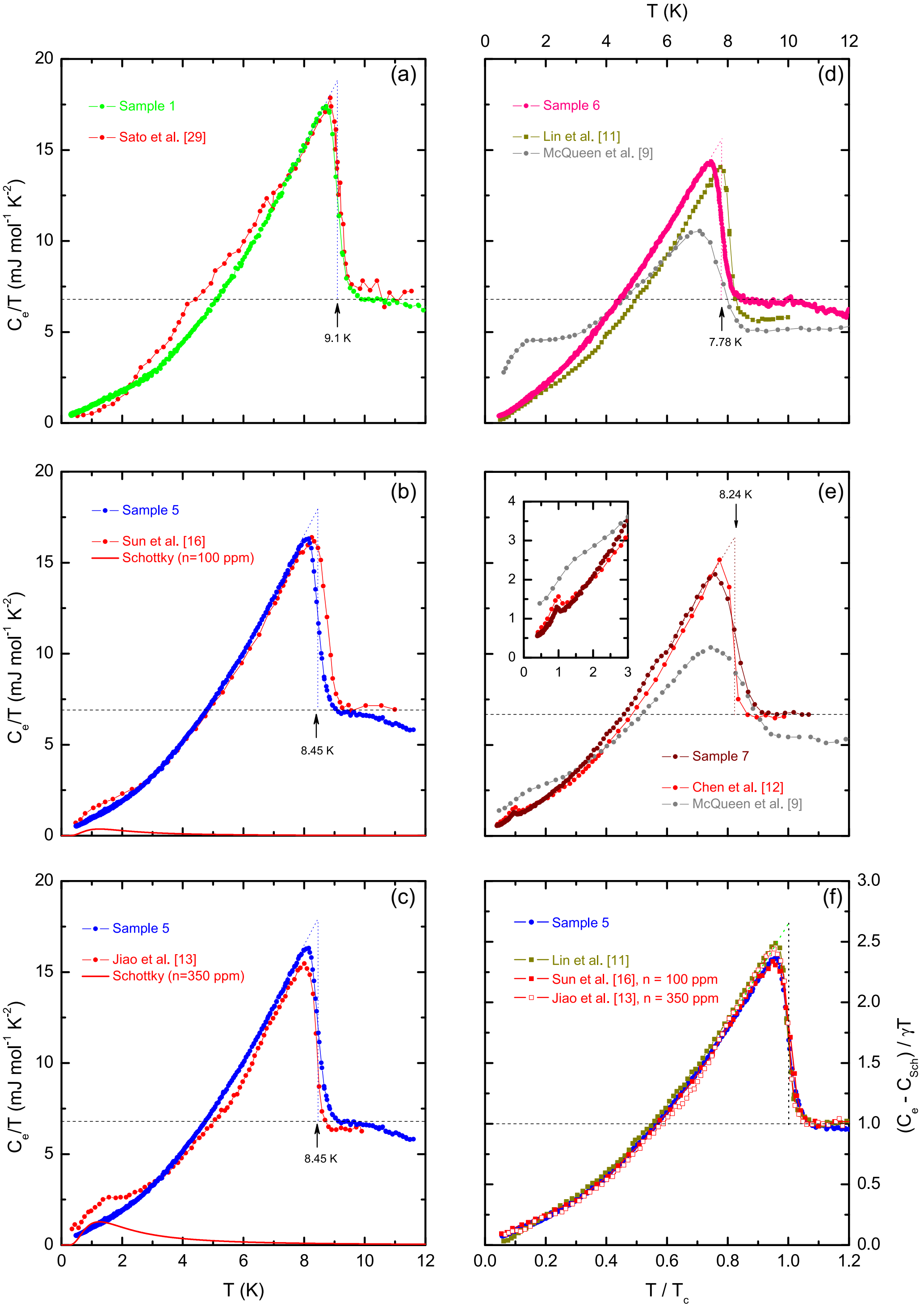

FIG. 7. Comparison of published $C_e(T)$ [samples grown by solid-state reaction (gray) [33], KCl : AlCl$_3$ flux (dark yellow) [21], and chemical vapor transport (red) [9,22–24,66]], to our samples with similar $T_c$ values. The inset shows data below 3 K on an enlarged scale. The dotted line is an entropy-conserving construction to determine $T_c$ in our samples. The continuous red lines shown in (b) and (c) are Schottky contributions $C_{\mathrm{Sch}}(T, n)$ calculated with Eq. (D1) for the samples of Sun *et al.* [24] and Jiao *et al.* [22], respectively. The difference $C_e(T) - C_{\mathrm{Sch}}(T, n)$ for both samples is compared in (f) to $C_e(T)$ of sample 5 and Lin *et al.* [21].

### 1. Two-band model (one hole and one electron bands)

In this case, $\alpha$ and $\gamma$ ($\beta$ and $\delta$) represent the extremal orbits of an electron (hole) corrugated Fermi-surface sheet. Since $m_c^\alpha \neq m_c^\gamma$ and $m_c^\beta \neq m_c^\delta$, the minimal tight-binding model that accounts for two orbits with different cyclotron masses is given by

$$\epsilon(k) = -2t(\cos(k_x a) + \cos(k_y b))(1 + \eta\cos(k_z c)) - 2t_z\cos(k_z c), \tag{E1}$$

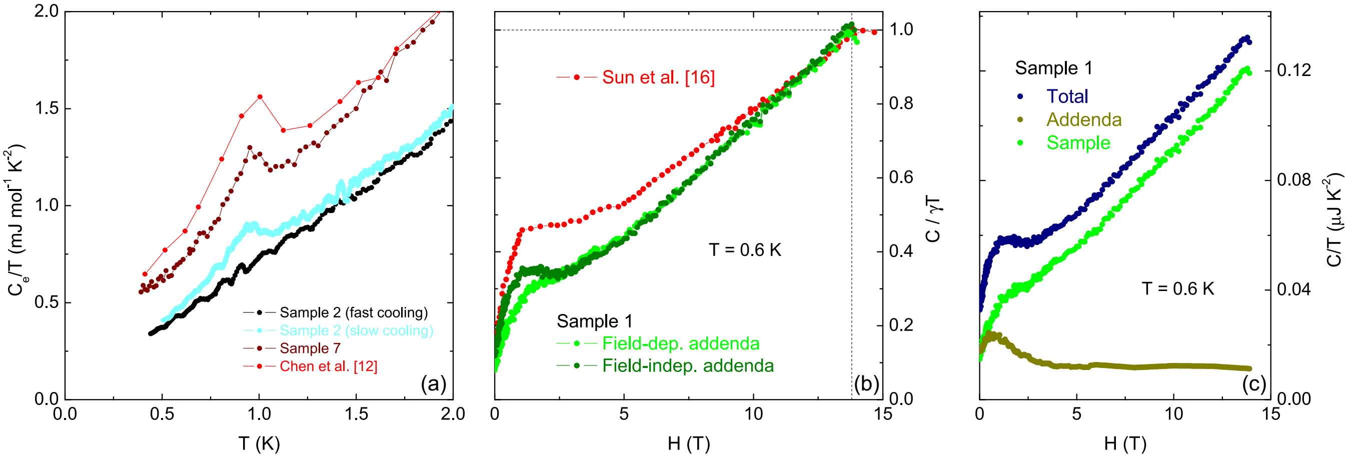

FIG. 8. (a) Comparison of the low temperature $C_e/T$ of samples 2 and 7 to that of Chen *et al.* [9]. The 1 K anomaly is only observed in our samples for measurements performed upon slow cooling. (b) Comparison of the mixed-state heat capacity reported by Sun *et al.* [24] (red curve) to that of sample 1 (light green curve). The dark green curve shows the erroneous heat capacity of sample 1 obtained when the field dependence of the addenda is not taken into account. (c) Field dependence of the addenda (dark yellow curve) and sample (light green curve) contributions to the total heat capacity (dark blue curve). We find that the addenda in our setup have a strong field dependence in low fields.

with $t > 0$ and $t_z > 0$. Since $k_F \ll \frac{\pi}{a}, \frac{\pi}{b}$, we can Taylor expand the cosines, which leads to

$$\epsilon(k) = -4t + \alpha\cos(k_z c) + \frac{\hbar^2}{2}\left(\frac{k_x^2}{m_x} + \frac{k_y^2}{m_y}\right)(1+\eta\cos(k_z c)), \tag{E2}$$

where $\frac{\hbar^2}{2m_x} = a^2 t$, $\frac{\hbar^2}{2m_y} = b^2 t$ and $\alpha = -2(t_z + 2\eta t)$. In the following, we can neglect $4t$ since it produces only a constant energy shift. In this approximation, the orbit area $A$ is given by

$$A = 2\pi\frac{\sqrt{m_x m_y}}{\hbar^2}\left(\frac{\epsilon - \alpha\cos(k_z c)}{1+\eta\cos(k_z c)}\right). \tag{E3}$$

Using the definition of $m_c = \frac{\hbar^2}{2\pi}\frac{\partial A}{\partial \epsilon}$ and the Onsager relation $F = \frac{\hbar}{2\pi e}A$, we get

$$m_c = \frac{\sqrt{m_x m_y}}{1+\eta\cos(k_z c)}, \tag{E4}$$

and

$$F = \frac{\sqrt{m_x m_y}}{\hbar e}\left(\frac{\epsilon_F - \alpha\cos(k_z c)}{1+\eta\cos(k_z c)}\right), \tag{E5}$$

under the condition that $\epsilon_F > \alpha$. Values of $\sqrt{m_x m_y}$, $\eta$, $\alpha$, $\epsilon_F$ for each sheet are obtained by replacing the experimental values of $m_c$ and $F$ in Eqs. (E4) and (E5) (see Table III). With these parameters, the Sommerfeld coefficient $\gamma_n$ of each band can be calculated using

$$\gamma_n = \frac{2\pi^2}{3}k_B^2 N(0), \tag{E6}$$

where

$$N(0) = \frac{1}{2\pi\hbar^2 c}\sqrt{\frac{m_x m_y}{1-\eta^2}} \tag{E7}$$

is the density of states (per spin orientation). Finally, the number of carriers is given by

$$n = \frac{1}{\pi\hbar^2 c}\sqrt{\frac{m_x m_y}{1-\eta^2}}\left(\epsilon_F + \frac{\alpha}{\eta}\left(1-\sqrt{1-\eta^2}\right)\right). \tag{E8}$$

As shown in Table III, we find that the carrier compensation is fulfilled within 1% error in this two-band model while the Sommerfeld coefficient amounts to 5.7 mJ mol$^{-1}$ K$^{-2}$. This value is smaller than our direct heat-capacity measurement by only about 17%. This scenario is compatible with the recent ARPES study of Watson *et al.* on detwinned single crystals, in which only one electron band was observed. [25]

TABLE III. The first four columns summarize the quantum-oscillation data from Ref. [45]. The next columns indicate the band-structure parameters inferred from our analysis within a two-band model. $m_e$ is the bare electron mass. The value of $k_z$ is arbitrarily chosen.

| Quantum oscillation | | | | Two-band model | | | | | | |
|---|---|---|---|---|---|---|---|---|---|---|
| Orbit | Carrier type | F (kT) | $\frac{m_c}{m_e}$ | $k_z$ | $\eta$ | $\alpha$ (meV) | $\frac{\sqrt{m_x m_y}}{m_e}$ | $\epsilon_F$ (meV) | $n$ (carrier/Fe) | $\gamma$ (mJ mol$^{-1}$ K$^{-2}$) |
| $\alpha$ | electron | 0.06 | 1.92 | 0 | 0.58 | 2.76 | 3.03 | 6.39 | 0.00802 | 2.6 |
| $\gamma$ | | 0.57 | 7.22 | $\frac{\pi}{c}$ | | | | | | |
| $\beta$ | hole | 0.20 | 4.31 | 0 | –0.01 | 6.64 | 4.27 | 12.02 | 0.00812 | 2.98 |
| $\delta$ | | 0.68 | 4.22 | $\frac{\pi}{c}$ | | | | | | |

TABLE IV. The first four columns summarize the quantum-oscillation data from Ref. [45]. The next columns indicate the band-structure parameters inferred from our analysis within a three-band model. $m_e$ is the bare electron mass. The value of $k_z$ is arbitrarily chosen.

| Quantum oscillation data | | | | Three-band model | | | | | | |
|---|---|---|---|---|---|---|---|---|---|---|
| Orbit | Carrier type | F (kT) | $\frac{m_c}{m_e}$ | $k_z$ | $\eta$ | $\alpha$ (meV) | $\frac{\sqrt{m_x m_y}}{m_e}$ | $\epsilon_F$ (meV) | $n$(carrier/Fe) | $\gamma$(mJ mol$^{-1}$ K$^{-2}$) |
| $\alpha$ | electron | 0.06 | 1.92 | - | - | - | 1.92 | 3.62 | 0.00206 | 1.34 |
| $\gamma$ | electron | 0.57 | 7.22 | - | - | - | 7.22 | 9.14 | 0.0196 | 5.04 |
| $\beta$ | hole | 0.20 | 4.31 | 0 | $-0.01$ | 6.64 | 4.27 | 12.02 | 0.00812 | 2.98 |
| $\delta$ | | 0.68 | 4.22 | $\frac{\pi}{c}$ | | | | | | |

### 2. Three-band model (one hole and two electron bands)

In this scenario, $\beta$ and $\delta$ are the extremal orbits of the hole corrugated sheet, whereas $\alpha$ and $\gamma$ represent the frequencies of two distinct 2D uncorrugated electron sheets. The results of the two-band model are unchanged for the hole pocket. However, for each electron sheet, the density of states and the carrier densities are given by the following expressions:

$$N(0) = \frac{\sqrt{m_x m_y}}{2\pi\hbar^2 c}, \tag{E9}$$

and

$$n = \frac{\sqrt{m_x m_y}}{\pi\hbar^2 c}\epsilon_F. \tag{E10}$$

As shown in Table IV, we obtain a Sommerfeld coefficient of about 9.36 mJ mol$^{-1}$ K$^{-2}$ within this three-band model, which is larger than our direct measurement by a factor 1.35. Also, the carrier compensation is clearly not fulfilled in this scenario.

---

[1] A. Chubukov, Annu. Rev. Condens. Matter Phys. **3**, 57 (2012).

[2] P. J. Hirschfeld, M. M. Korshunov, and I. I. Mazin, Rep. Prog. Phys. **74**, 124508 (2011).

[3] P. J. Hirschfeld, Iron-based superconductors/Supraconducteurs à base de fer, C. R. Phys. **17**, 197 (2016).

[4] A. E. Böhmer and A. Kreisel, J. Phys.: Condens. Matter **30**, 023001 (2018).

[5] A. I. Coldea and M. D. Watson, Annu. Rev. Condens. Matter Phys. **9**, 125 (2018).

[6] L. Fanfarillo, J. Mansart, P. Toulemonde, H. Cercellier, P. Le Fèvre, F. Bertran, B. Valenzuela, L. Benfatto, and V. Brouet, Phys. Rev. B **94**, 155138 (2016).

[7] D. F. Agterberg, T. M. Rice, and M. Sigrist, Phys. Rev. Lett. **78**, 3374 (1997).

[8] P. O. Sprau, A. Kostin, A. Kreisel, A. E. Böhmer, V. Taufour, P. C. Canfield, S. Mukherjee, P. J. Hirschfeld, B. M. Andersen, and J. C. S. Davis, Science **357**, 75 (2017).

[9] G.-Y. Chen, X. Zhu, H. Yang, and H.-H. Wen, Phys. Rev. B **96**, 064524 (2017).

[10] T. Hashimoto, Y. Ota, H. Q. Yamamoto, Y. Suzuki, T. Shimojima, S. Watanabe, C. Chen, S. Kasahara, Y. Matsuda, T. Shibauchi, K. Okazaki, and S. Shin, Nat. Commun. **9**, 282 (2018).

[11] D. Liu, C. Li, J. Huang, B. Lei, L. Wang, X. Wu, B. Shen, Q. Gao, Y. Zhang, X. Liu, Y. Hu, Y. Xu, A. Liang, J. Liu, P. Ai, L. Zhao, S. He, L. Yu, G. Liu, Y. Mao, X. Dong, X. Jia, F. Zhang, S. Zhang, F. Yang, Z. Wang, Q. Peng, Y. Shi, J. Hu, T. Xiang, X. Chen, Z. Xu, C. Chen, and X. J. Zhou, Phys. Rev. X **8**, 031033 (2018).

[12] Y. S. Kushnirenko, A. V. Fedorov, E. Haubold, S. Thirupathaiah, T. Wolf, S. Aswartham, I. Morozov, T. K. Kim, B. Büchner, and S. V. Borisenko, Phys. Rev. B **97**, 180501 (2018).

[13] L. C. Rhodes, M. D. Watson, A. A. Haghighirad, D. V. Evtushinsky, M. Eschrig, and T. K. Kim, Phys. Rev. B **98**, 180503 (2018).

[14] A. Kreisel, B. M. Andersen, P. O. Sprau, A. Kostin, J. C. Seamus Davis, and P. J. Hirschfeld, Phys. Rev. B **95**, 174504 (2017).

[15] J. Kang, R. M. Fernandes, and A. V. Chubukov, Phys. Rev. Lett. **120**, 267001 (2018).

[16] L. Benfatto, B. Valenzuela, and L. Fanfarillo, NPJ Quantum Mater. **3**, 56 (2018).

[17] J. K. Dong, T. Y. Guan, S. Y. Zhou, X. Qiu, L. Ding, C. Zhang, U. Patel, Z. L. Xiao, and S. Y. Li, Phys. Rev. B **80**, 024518 (2009).

[18] P. Bourgeois-Hope, S. Chi, D. A. Bonn, R. Liang, W. N. Hardy, T. Wolf, C. Meingast, N. Doiron-Leyraud, and L. Taillefer, Phys. Rev. Lett. **117**, 097003 (2016).

[19] M. Li, N. R. Lee-Hone, S. Chi, R. Liang, W. N. Hardy, D. A. Bonn, E. Girt, and D. M. Broun, New J. Phys. **18**, 082001 (2016).

[20] S. Teknowijoyo, K. Cho, M. A. Tanatar, J. Gonzales, A. E. Böhmer, O. Cavani, V. Mishra, P. J. Hirschfeld, S. L. Bud'ko, P. C. Canfield, and R. Prozorov, Phys. Rev. B **94**, 064521 (2016).

[21] J.-Y. Lin, Y. S. Hsieh, D. A. Chareev, A. N. Vasiliev, Y. Parsons, and H. D. Yang, Phys. Rev. B **84**, 220507 (2011).

[22] L. Jiao, C.-L. Huang, S. Rößler, C. Koz, U. K. Rößler, U. Schwarz, and S. Wirth, Sci. Rep. **7**, 44024 (2017).

[23] Y. Sato, S. Kasahara, T. Taniguchi, X. Xing, Y. Kasahara, Y. Tokiwa, Y. Yamakawa, H. Kontani, T. Shibauchi, and Y. Matsuda, Proc. Natl. Acad. of Sci. **115**, 1227 (2018).

[24] Y. Sun, S. Kittaka, S. Nakamura, T. Sakakibara, K. Irie, T. Nomoto, K. Machida, J. Chen, and T. Tamegai, Phys. Rev. B **96**, 220505 (2017).

[25] M. D. Watson, A. A. Haghighirad, L. C. Rhodes, M. Hoesch, and T. K. Kim, New J. Phys. **19**, 103021 (2017).

[26] T. Watashige, Y. Tsutsumi, T. Hanaguri, Y. Kohsaka, S. Kasahara, A. Furusaki, M. Sigrist, C. Meingast, T. Wolf, H. v. Löhneysen, T. Shibauchi, and Y. Matsuda, Phys. Rev. X **5**, 031022 (2015).

[27] X. F. Wang, T. Wu, G. Wu, H. Chen, Y. L. Xie, J. J. Ying, Y. J. Yan, R. H. Liu, and X. H. Chen, Phys. Rev. Lett. **102**, 117005 (2009).

[28] A. E. Böhmer, V. Taufour, W. E. Straszheim, T. Wolf, and P. C. Canfield, Phys. Rev. B **94**, 024526 (2016).

[29] S. Rößler, C.-L. Huang, L. Jiao, C. Koz, U. Schwarz, and S. Wirth, Phys. Rev. B **97**, 094503 (2018).

[30] F. Hardy, P. Burger, T. Wolf, R. A. Fisher, P. Schweiss, P. Adelmann, R. Heid, R. Fromknecht, R. Eder, D. Ernst, H. v. Löhneysen, and C. Meingast, EPL **91**, 47008 (2010).

[31] F. Bouquet, Y. Wang, R. A. Fisher, D. G. Hinks, J. D. Jorgensen, A. Junod, and N. E. Phillips, Europhys. Lett. **56**, 856 (2001).

[32] F. Hardy, R. Eder, M. Jackson, D. Aoki, C. Paulsen, T. Wolf, P. Burger, A. Böhmer, P. Schweiss, P. Adelmann, R. A. Fisher, and C. Meingast, J. Phys. Soc. Jpn. **83**, 014711 (2014).

[33] T. M. McQueen, Q. Huang, V. Ksenofontov, C. Felser, Q. Xu, H. Zandbergen, Y. S. Hor, J. Allred, A. J. Williams, D. Qu, J. Checkelsky, N. P. Ong, and R. J. Cava, Phys. Rev. B **79**, 014522 (2009).

[34] G. E. Volovik, JETP Lett. **58**, 469 (1993).

[35] C. Kübert and P. Hirschfeld, Solid State Commun. **105**, 459 (1998).

[36] I. Vekhter, P. J. Hirschfeld, and E. J. Nicol, Phys. Rev. B **64**, 064513 (2001).

[37] Y. Wang, B. Revaz, A. Erb, and A. Junod, Phys. Rev. B **63**, 094508 (2001).

[38] M. Ichioka and K. Machida, Phys. Rev. B **76**, 064502 (2007).

[39] K. Machida and M. Ichioka, Phys. Rev. B **77**, 184515 (2008).

[40] L. Jiao, S. Rößler, C. Koz, U. Schwarz, D. Kasinathan, U. K. Rößler, and S. Wirth, Phys. Rev. B **96**, 094504 (2017).

[41] V. Mishra, G. R. Boyd, S. Graser, T. Maier, P. J. Hirschfeld, and D. J. Scalapino, Phys. Rev. B **79**, 094512 (2009).

[42] V. Mishra, A. Vorontsov, P. J. Hirschfeld, and I. Vekhter, Phys. Rev. B **80**, 224525 (2009).

[43] A. Fedorov, A. Yaresko, T. K. Kim, Y. Kushnirenko, E. Haubold, T. Wolf, M. Hoesch, A. Grüneis, B. Büchner, and S. V. Borisenko, Sci. Rep. **6**, 36834 (2016).

[44] V. Barzykin and L. P. Gor'kov, Phys. Rev. B **76**, 014509 (2007).

[45] T. Terashima, N. Kikugawa, A. Kiswandhi, E.-S. Choi, J. S. Brooks, S. Kasahara, T. Watashige, H. Ikeda, T. Shibauchi, Y. Matsuda, T. Wolf, A. E. Böhmer, F. Hardy, C. Meingast, H. v. Löhneysen, M.-T. Suzuki, R. Arita, and S. Uji, Phys. Rev. B **90**, 144517 (2014).

[46] T. Terashima, N. Kurita, M. Tomita, K. Kihou, C.-H. Lee, Y. Tomioka, T. Ito, A. Iyo, H. Eisaki, T. Liang, M. Nakajima, S. Ishida, S.-i. Uchida, H. Harima, and S. Uji, Phys. Rev. Lett. **107**, 176402 (2011).

[47] L. de' Medici, G. Giovannetti, and M. Capone, Phys. Rev. Lett. **112**, 177001 (2014).

[48] S. Backes, H. O. Jeschke, and R. Valentí, Phys. Rev. B **92**, 195128 (2015).

[49] F. Eilers, K. Grube, D. A. Zocco, T. Wolf, M. Merz, P. Schweiss, R. Heid, R. Eder, R. Yu, J.-X. Zhu, Q. Si, T. Shibauchi, and H. v. Löhneysen, Phys. Rev. Lett. **116**, 237003 (2016).

[50] F. Hardy, A. E. Böhmer, L. de' Medici, M. Capone, G. Giovannetti, R. Eder, L. Wang, M. He, T. Wolf, P. Schweiss, R. Heid, A. Herbig, P. Adelmann, R. A. Fisher, and C. Meingast, Phys. Rev. B **94**, 205113 (2016).

[51] F. Hardy, A. E. Böhmer, D. Aoki, P. Burger, T. Wolf, P. Schweiss, R. Heid, P. Adelmann, Y. X. Yao, G. Kotliar, J. Schmalian, and C. Meingast, Phys. Rev. Lett. **111**, 027002 (2013).

[52] K. Haule and G. Kotliar, New J. Phys. **11**, 025021 (2009).

[53] S. Karlsson, P. Strobel, A. Sulpice, C. Marcenat, M. Legendre, F. Gay, S. Pairis, O. Leynaud, and P. Toulemonde, Supercond. Sci. Technol. **28**, 105009 (2015).

[54] D. Chareev, E. Osadchii, T. Kuzmicheva, J.-Y. Lin, S. Kuzmichev, O. Volkova, and A. Vasiliev, Cryst. Eng. Comm. **15**, 1989 (2013).

[55] A. E. Böhmer, F. Hardy, F. Eilers, D. Ernst, P. Adelmann, P. Schweiss, T. Wolf, and C. Meingast, Phys. Rev. B **87**, 180505 (2013).

[56] S. Kasahara, T. Watashige, T. Hanaguri, Y. Kohsaka, T. Yamashita, Y. Shimoyama, Y. Mizukami, R. Endo, H. Ikeda, K. Aoyama, T. Terashima, S. Uji, T. Wolf, H. von Löhneysen, T. Shibauchi, and Y. Matsuda, Proc. Natl. Acad. Sci. **111**, 16309 (2014).

[57] R. Bachmann, F. J. DiSalvo Jr., T. H. Geballe, R. L. Greene, R. E. Howard, C. N. King, H. C. Kirsch, K. N. Lee, R. E. Schwall, H. Thomas, and R. B. Zubeck, Rev. Sci. Instrum. **43**, 205 (1972).

[58] C. Marcenat, Etude Calorimétrique Sous Champ Magnétique des Phases Basses Températures des Composés Kondo Ordonnés:$CeB_6$ et TmS, Ph.D. thesis, Université scientifique et Médicale de Grenoble, 1986.

[59] S. Riegel and G. Weber, J. Phys. E **19**, 790 (1986).

[60] N. E. Phillips, C. R. C. Crit. Rev. Solid State Sci. **2**, 467 (1971).

[61] C. R. Rotundu, T. R. Forrest, N. E. Phillips, and R. J. Birgeneau, J. Phys. Soc. Jpn. **84**, 114701 (2015).

[62] A. Williams, T. McQueen, and R. Cava, Solid State Commun. **149**, 1507 (2009).

[63] C. Koz, M. Schmidt, H. Borrmann, U. Burkhardt, S. Rößler, W. Carrillo-Cabrera, W. Schnelle, U. Schwarz, and Y. Grin, Z. Anorg. Allg. Chem. **640**, 1600 (2014).

[64] S. Rößler, C. Koz, S. Wirth, and U. Schwarz, Phys. Status Solidi (b) **254**, 1600149 (2017).

[65] Y. Sun, S. Pyon, T. Tamegai, R. Kobayashi, T. Watashige, S. Kasahara, Y. Matsuda, and T. Shibauchi, Phys. Rev. B **92**, 144509 (2015).

[66] Y. Sun, A. Park, S. Pyon, T. Tamegai, and H. Kitamura, Phys. Rev. B **96**, 140505 (2017).

[67] M. D. Watson, T. Yamashita, S. Kasahara, W. Knafo, M. Nardone, J. Béard, F. Hardy, A. McCollam, A. Narayanan, S. F. Blake, T. Wolf, A. A. Haghighirad, C. Meingast, A. J. Schofield, H. v. Löhneysen, Y. Matsuda, A. I. Coldea, and T. Shibauchi, Phys. Rev. Lett. **115**, 027006 (2015).

[68] M. D. Watson, T. K. Kim, A. A. Haghighirad, N. R. Davies, A. McCollam, A. Narayanan, S. F. Blake, Y. L. Chen, S. Ghannadzadeh, A. J. Schofield, M. Hoesch, C. Meingast, T. Wolf, and A. I. Coldea, Phys. Rev. B **91**, 155106 (2015).

[69] A. Audouard, F. Duc, L. Drigo, P. Toulemonde, S. Karlsson, P. Strobel, and A. Sulpice, Europhys. Lett. **109**, 27003 (2015).